






Role of magnetic anisotropy in the antiskyrmion-host schreibersite magnets

M. Hemmida ¹, J. Masell ^{2,3}, K. Karube,³ D. Ehlers,¹ H.-A. Krug von Nidda ¹, V. Tsurkan,^{1,4} Y. Tokura ^{3,5,6},
Y. Taguchi ³ and I. Kézsmárki¹

¹Experimental Physics V, Center for Electronic Correlations and Magnetism, University of Augsburg, D-86135 Augsburg, Germany

²Institute of Theoretical Solid State Physics, Karlsruhe Institute of Technology (KIT), 76049 Karlsruhe, Germany

³RIKEN Center for Emergent Matter Science (CEMS), Wako 351-0198, Japan

⁴Institute of Applied Physics, Moldova State University, MD-2028 Chişinău, Republic of Moldova

⁵Department of Applied Physics and Quantum-Phase Electronics Center (QPEC), University of Tokyo, Tokyo 113-8656, Japan

⁶Tokyo College, University of Tokyo, Tokyo 113-8656, Japan



(Received 25 April 2024; accepted 23 July 2024; published 8 August 2024)

Magnetic anisotropy is a fundamental property of magnetic materials that plays an essential role in the stability of magnetic domains and skyrmions. In this ferromagnetic resonance study, we report the evolution of magnetic anisotropy by substituting various $4d$ metals in the antiskyrmion host $(\text{Fe}, \text{Ni})_3\text{P}$ with S_4 tetragonal symmetry. In the undoped compound $(\text{Fe}_{0.63}\text{Ni}_{0.37})_3\text{P}$ and in the Ru-doped $(\text{Fe}_{0.59}\text{Ni}_{0.32}\text{Ru}_{0.09})_3\text{P}$, the uniaxial magnetic anisotropy has an easy-plane character, while Pd doping turns the material to an easy-axis-type magnet, as observed in $(\text{Fe}_{0.62}\text{Ni}_{0.29}\text{Pd}_{0.09})_3\text{P}$. In addition to the dominant uniaxial anisotropy, we also quantify the fourfold anisotropy of the plane perpendicular to the tetragonal axis in $(\text{Fe}_{0.63}\text{Ni}_{0.30}\text{Pd}_{0.07})_3\text{P}$. Using analytical calculations and micromagnetic simulations, we discuss how this planar anisotropy competes with the anisotropic Dzyaloshinskii-Moriya interaction in determining the orientation of the magnetic stripes and the antiskyrmions.

DOI: [10.1103/PhysRevB.110.054416](https://doi.org/10.1103/PhysRevB.110.054416)

I. INTRODUCTION

During the last decade, extensive experimental and theoretical studies of several skyrmion-host materials revealed the important role of magnetocrystalline anisotropy in the formation and stability of the skyrmion lattice (SkL). In general, SkL phases are observed in noncentrosymmetric magnetic crystals, where due to the lack of inversion symmetry the Dzyaloshinskii-Moriya interaction (DMI) [1,2] gives rise to spin canting, resulting in spiral spin structures. Upon application of an external magnetic field, these spiral structures transform into a SkL, which exists in a certain field and temperature range, before it undergoes further metamagnetic transitions to the ferromagnetically (FM) polarized state at higher fields.

Recently, the role of magnetic anisotropy has been studied in various skyrmion hosts. In cubic chiral magnets such as MnSi, a Bloch-type hexagonal SkL arises from the zero-field helical spin structure within a small temperature range just below the ordering temperature. The SkL aligns with the skyrmion axes parallel to the external field and further transforms into a conical structure with increasing field [3]. Systematic investigations of the magnetic anisotropy were performed in $\text{Mn}_{1-x}\text{Fe}_x\text{Si}$, $\text{Mn}_{1-x}\text{Co}_x\text{Si}$ [4], FeGe [5], and Cu_2OSeO_3 [6,7]. Especially in the latter one, the most interesting observation concerned the formation of an additional low-temperature SkL state, when the tilted conical state gets destabilized above certain magnetic fields applied along one of the cubic [100] axes, which is the easy axis of magnetic anisotropy. In the β -Mn-type series $(\text{Co}_{0.5}\text{Zn}_{0.5})_{20-x}\text{Mn}_x$, the increase of the magnetic anisotropy to low temperatures was shown to result in a strong deformation of the skyrmion shape

[8]. In addition to the plethora of DMI-induced SkL states, skyrmions have been reported to emerge via the competition of easy-axis anisotropy and dipolar interactions [9–12], as well as via exchange frustration [13–17]. In these latter cases, anisotropy was also playing a vital role in the formation of twisted spin textures.

Even stronger is the influence of magnetic anisotropy in skyrmion hosts with C_{nv} symmetry, where the existence of a Néel-type SkL was already predicted more than 30 years ago [18] and recently observed in the polar magnetic semiconductors GaV_4S_8 , GaV_4Se_8 , and GaMo_4S_8 [19–25]. In these systems, the cubic high-temperature phase undergoes a Jahn-Teller transition between 40 and 50 K, resulting in a polar rhombohedral state with C_{nv} symmetry. The DMI vector pattern characteristic of the polar rhombohedral state stabilizes spin cycloids, in contrast to the spin helices observed in chiral magnets. Above a certain magnetic field, the Néel-type SkL is formed with the skyrmions axes parallel to the rhombohedral axis, followed by the FM polarized phase at higher fields. The extension of the SkL phase in the magnetic phase diagram strongly depends on the strength and the character (easy axis or easy plane) of the magnetic anisotropy and the direction of the magnetic field.

Very recently, the discovery of antiskyrmions in tetragonal Heusler systems Mn-Pt(Pd)-Sn [26,27] and Mn-Ni(Pd)-Ga [28–31] with D_{2d} symmetry has attracted great attention. An antiskyrmion, in contrast to vortexlike skyrmions, has antivortexlike character. Unlike a skyrmion, it does not have a unique chirality, but its chirality is direction dependent, dictated by the chirality of the DMI [26]. Similar to skyrmion host materials [32–34], antiskyrmion hosts show interesting physical properties such as the topological Hall effect [35,36].

Bulk $\text{Mn}_{1.4}\text{PtSn}$ exhibits a highly anisotropic topological Hall effect, which survives in the whole temperature range where the spin structure is noncoplanar ($T < 170$ K) [37]. Above the spin-reorientation temperature $T_{\text{SR}} = 170$ K, an anisotropic fractal magnetic domain pattern of closure domains is transformed into a set of bubble domains, whereas thin plates of the same compound exhibit an antiskyrmion lattice or helix structures [38]. In thin films of Mn_xPtSn ($1.48 \leq x \leq 2.04$), the fundamental exchange parameters are tunable by chemical substitution and thickness [39], reflected in the chiral-type Hall effect and the magnetic transitions [40,41]. In the proximity of T_{SR} , the evolution of the in-plane uniaxial anisotropy of Mn_xPtSn ($x = 1.0\text{--}1.6$) reflects the coexistence of the collinear and noncoplanar magnetic phases [42].

From the above, it is clear that the bubbles are stabilized by dipolar interactions and the role of the DMI term is limited to the determination if the bubbles are topologically trivial, Bloch-type skyrmionic bubbles, or antiskyrmionic ones. Like for the formation of skyrmions [7,8,43–45], magnetic anisotropy is decisive by controlling the formation of antiskyrmions [46–52]. Recently, the impact of the magnetic anisotropy on the formation of antiskyrmions has been demonstrated with the doping of some $4d$ elements into schreibersite $(\text{Fe,Ni})_3\text{P}$ [53–58]. Schreibersite $(\text{Fe,Ni})_3\text{P}$ exhibits a noncentrosymmetric tetragonal crystal structure with the space group $\bar{I}4$ of S_4 symmetry class. It possesses three inequivalent crystallographic (Fe,Ni) sites. A twofold rotation symmetry around the $[100]$ and $[010]$ axes and a mirror symmetry with respect to the (110) and $(\bar{1}10)$ planes are absent in the S_4 symmetry, which results in a symmetry lower than D_{2d} [53]. Fe_3P exhibits strong easy-plane anisotropy, which is weakened by partial substitution of Fe by Ni. At close to 40% Ni, the easy-plane anisotropy reaches a minimum. Additional substitution of Fe by a few percent of Pd switches the anisotropy into easy axis, allowing for the formation of antiskyrmions. Accompanied by micromagnetic simulations, the formation of antiskyrmions or skyrmions in schreibersite was studied dependent on the character of the anisotropy induced by controlled substitution of $4d$ elements [54].

In the present work, we applied the ferromagnetic resonance (FMR) technique at 9.4 GHz in order to refine the analysis of the temperature dependence of uniaxial anisotropy in $(\text{Fe}_{0.63}\text{Ni}_{0.37})_3\text{P}$, $(\text{Fe}_{0.59}\text{Ni}_{0.32}\text{Ru}_{0.09})_3\text{P}$, and $(\text{Fe}_{0.62}\text{Ni}_{0.29}\text{Pd}_{0.09})_3\text{P}$, as well as the basal-plane anisotropy in $(\text{Fe}_{0.63}\text{Ni}_{0.30}\text{Pd}_{0.07})_3\text{P}$. In addition to our previous analysis based mainly on magnetization measurements, our present study allows one to resolve higher-order uniaxial anisotropy contributions K_2 and K_3 beyond the leading contribution of K_1 . In addition, we performed micromagnetic simulations to understand the impact of the fourfold planar anisotropy K_b on the orientation of the stripe phase and domain walls.

II. THE IMPACT OF MAGNETOCRYSTALLINE ANISOTROPIES ON FMR EXPERIMENTS: A BRIEF OVERVIEW

A. Theory

The effect of the magnetic domainlike structures on the FMR experiments in materials with magnetocrystalline

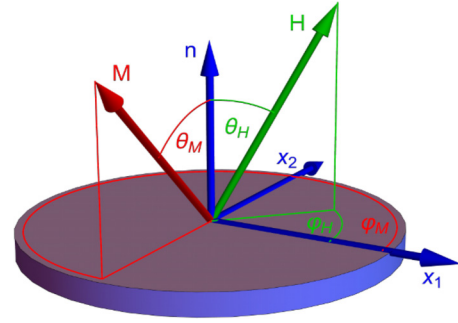


FIG. 1. Spherical coordinate system used for modeling of FMR in the case of an ellipsoid of revolution, which is well approximated by a cylindrical thin disk. The orientations of the DC magnetic field \mathbf{H} and magnetization \mathbf{M} are described by angles (θ_H, φ_H) and (θ_M, φ_M) , respectively. The choice of crystallographic axes (x_1, x_2, \mathbf{n}) depends on the individual experimental setup (see Fig. 2).

anisotropies was studied by Smit and Beljers [59] and Suhl [60]. They considered the case where the single-crystalline sample has the form of an ellipsoid of revolution, as shown in the schematic picture in Fig. 1. The anisotropy of the resonance fields H_{res} can be simulated using the Smit-Beljers-Suhl formula [59,60],

$$\left[\frac{\omega}{\gamma} \right]^2 = \frac{1}{M_s^2 \sin^2 \theta_M} \left[\frac{\partial^2 F}{\partial \theta_M^2} \frac{\partial^2 F}{\partial \varphi_M^2} - \left(\frac{\partial^2 F}{\partial \theta_M \partial \varphi_M} \right)^2 \right], \quad (1)$$

where F is the total magnetic free-energy density. The quantities ω , γ , and M_s are the angular frequency, the gyromagnetic ratio, and the saturation magnetization, respectively. The magnetization vector \mathbf{M} is parametrized by polar angle θ_M and the azimuthal angle φ_M within a spherical coordinate system. Note that due to the presence of magnetic anisotropies, the equilibrium orientation of the magnetization can deviate from the direction of the external field \mathbf{H} given by (θ_H, φ_H) (Fig. 1). The actual orientation of \mathbf{M} is found by minimizing the free energy as $\partial F / \partial \theta_M = 0$ and $\partial F / \partial \varphi_M = 0$.

Now we consider $F = F_{\text{Zee}} + F_{\text{dem}} + F_{\text{ani}}$, where the first two terms include the contribution of the Zeeman energy, $F_{\text{Zee}} = -\mathbf{M} \cdot \mathbf{H}$, and the demagnetization factor, $F_{\text{dem}} = \frac{1}{2} N_{\text{eff}} M^2 \cos^2 \theta_M$. The effective demagnetization factor is given as $N_{\text{eff}} = N_z - N_x$ for the FMR experiments, if a cylindrical thin disk is used, where the demagnetization factor remains unchanged upon the field rotation around its symmetry axis (z axis), as depicted in Fig. 1, and is computed according to Ref. [61], in which the ratio of diameter/thickness (d/h) is taken into account.

Based on the S_4 symmetry of the considered materials, the magnetocrystalline anisotropy reads up to six order as

$$F_{\text{ani}} = -(K_1 \mathbf{m}_z^2 + K_2 \mathbf{m}_z^4 + K_3 \mathbf{m}_z^6) - K_b (\hat{\mathbf{b}}_1 \cdot \mathbf{m})^2 (\hat{\mathbf{b}}_2 \cdot \mathbf{m})^2, \quad (2)$$

where $\mathbf{m} = \mathbf{M}/M_s$ is the reduced magnetization, \mathbf{m}_z denotes the magnetization component parallel to the roto-inversion axis of the S_4 symmetry, i.e., the $[001]$ axis, K_i are the uniaxial anisotropy constants of increasing order ($i = 1, 2, 3$), and K_b denotes the basal anisotropy. The defining axes $\hat{\mathbf{b}}_1$ and $\hat{\mathbf{b}}_2$ together with $\langle 001 \rangle$ form an orthonormal basis. Due to the low symmetry of S_4 , the directions of $\hat{\mathbf{b}}_1$ and $\hat{\mathbf{b}}_2$ in the basal plane

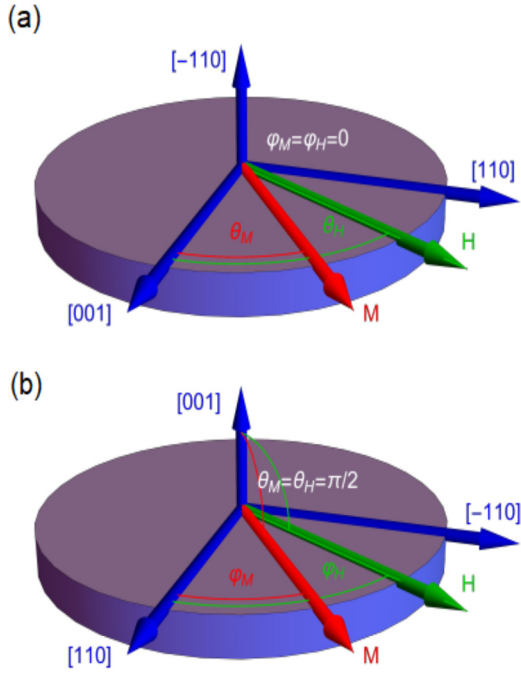


FIG. 2. Experimental setups: (a) a disk with $\mathbf{x}_1 = [001]$ and $\mathbf{x}_2 = [110]$ was used for uniaxial anisotropy measurements, and (b) a disk with $\mathbf{x}_1 = [110]$ and $\mathbf{x}_2 = [\bar{1}10]$ was used for basal anisotropy measurements.

are not constrained by symmetry and are determined by details of the unit cell, similar to the orientation of the antisymmetric DMI in this system [53]. This is in contrast to more symmetric systems such as D_{2d} , where extra mirror planes fix the orientation of the DMI and basal anisotropy. In the following, we define the basal axes with respect to the crystallographic $\langle 100 \rangle$ and $\langle 010 \rangle$ directions via $\hat{\mathbf{b}}_1 = \cos \varphi_b \hat{e}_{100} + \sin \varphi_b \hat{e}_{010}$ and $\hat{\mathbf{b}}_2 = \hat{e}_{001} \times \hat{\mathbf{b}}_1$.

1. Uniaxial anisotropy

For measurements of the uniaxial anisotropy, we consider a disk-shaped sample with the $\mathbf{x}_1 = [001]$ and $\mathbf{x}_2 = [110]$ axes; see Fig. 2(a). Note that here the polar angles θ_M and θ_H are not defined with respect to the rotational axis, but to the crystallographic axis of highest symmetry, $\mathbf{x}_1 = [001]$. With the rotational axis $\mathbf{n} = [\bar{1}10]$, the azimuthal angles φ_M and φ_H are fixed to zero.

In the case of a tetragonal crystal structure with uniaxial symmetry, the first three terms of the anisotropy energy F_{ani} in Eq. (2) can be rewritten as follows [62,63]:

$$F_{\text{ani}} = K_1 \sin^2 \theta_M + K_2 \sin^4 \theta_M + K_3 \sin^6 \theta_M, \quad (3)$$

where the magnetic anisotropy energy depends only on the polar angle (θ_M) between the magnetic moment and the crystallographic axis of highest symmetry. Usually, the anisotropy constants K_2 (fourth order) and K_3 (sixth order) are at least one order of magnitude smaller than K_1 (second order) [62]. In the case of $K_u > 0$, the anisotropy is of easy-axis type, whereas $K_u < 0$ for the easy-plane-type anisotropy. Here, K_u is the total uniaxial anisotropy. Due to their small contributions, the higher-order anisotropy terms in Eq. (3) are usually neglected,

i.e., $K_u \approx K_1$. We can calculate the anisotropy field, which is a measure of energy difference between the hard and easy directions, as $H_{\text{ani}} = (1/M_s)(\partial^2 F_{\text{ani}}/\partial \theta_M^2)$. Following Eq. (3), for $\theta_M = 0$, one obtains [63]

$$H_{\text{ani}} = \frac{2K_1}{M_s}. \quad (4)$$

2. Basal anisotropy

For measurements of the basal anisotropy, we consider a disk-shaped sample with the $\mathbf{x}_1 = [110]$ and $\mathbf{x}_2 = [\bar{1}10]$ axes; see Fig. 2(b). Here the rotational axis $\mathbf{n} = [001]$ corresponds to the crystallographic axis of highest symmetry.

The total energy density $F = F_{\text{dem}} + F_{\text{Zee}} + F_{\text{ani}}$ for an external field \mathbf{H} in the plane of the disk comprises the demagnetization energy F_{dem} , the Zeeman energy $F_{\text{Zee}} = -HM_s \cos(\varphi_H - \varphi_M) \sin \theta_M$, and the anisotropy energy,

$$F_{\text{ani}} = -K_1 \cos^2 \theta_M - K_2 \cos^4 \theta_M - \frac{K_b}{4} \cos^2[2(\varphi_b - \varphi_M)] \sin^4 \theta_M, \quad (5)$$

where we neglected terms with K_3 as they are small. From Eq. (1) follows, in the limit of large field $M_s H_{\text{res}} \gg |\mu_0 M_s^2 N_{\text{eff}} - 2K_1| \gg |K_b|, |K_2|$, the resonance field

$$\mu_0 H_{\text{res}} = \frac{\omega}{\gamma} - \frac{\mu_0 M_s}{2} N_{\text{eff}} + \frac{K_1}{M_s} - \frac{K_b}{4M_s} \{1 + 5 \cos[4(\varphi_H) - \varphi_b]\}, \quad (6)$$

which is independent of K_2 . The basal anisotropy K_b causes a fourfold periodic pattern in the resonance spectrum with a phase shift that allows one to determine the basal axis orientation φ_b . By taking the difference of the maximal and minimal resonance fields, we can determine the magnitude of the basal anisotropy,

$$\Delta H_{\text{res}} = H_{\text{res}}^{\text{max}} - H_{\text{res}}^{\text{min}} = \frac{5|K_b|}{2\mu_0 M_s}. \quad (7)$$

Due to small but finite unavoidable misalignments of the sample, the rotation plane of the magnetic field does not perfectly coincide with the basal plane. This can lead to the intermixing of the uniaxial anisotropy with the basal-plane anisotropy. As a consequence, the angular dependence of the resonance field would not show a $\pi/2$ periodicity, but would acquire a π periodic term due to the uniaxial anisotropy. In particular, if the crystallographic axes are tilted with respect to the disk axis by the polar angle θ_t for the azimuth angle φ_t , the resonance field becomes

$$\mu_0 H_{\text{res}} \approx \frac{\omega}{\gamma} - \frac{\mu_0 M_s}{2} N_{\text{eff}} + \left(1 - \frac{3}{2} \theta_t^2\right) \frac{K_1}{M_s} - \frac{K_b}{4M_s} + \frac{3K_1 \theta_t^2}{2M_s} \cos[2(\varphi_H - \varphi_t)] - \frac{5K_b}{4M_s} \cos[4(\varphi_H - \varphi_b)], \quad (8)$$

where contributions other than K_1 and K_b have been neglected. Thus, we can determine K_b by fitting a sum of trigonometric functions with individual phase shifts to the resonance spectrum.

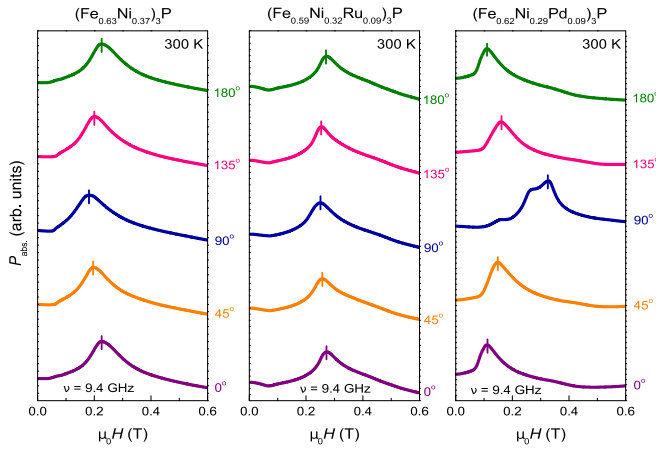


FIG. 3. Selected FMR spectra of $(\text{Fe}_{0.63}\text{Ni}_{0.37})_3\text{P}$, $(\text{Fe}_{0.59}\text{Ni}_{0.32}\text{Ru}_{0.09})_3\text{P}$, and $(\text{Fe}_{0.62}\text{Ni}_{0.29}\text{Pd}_{0.09})_3\text{P}$ at 300 K and various orientations of the magnetic field. The spectra represent the absorbed microwave power (P_{abs}) as a function of magnetic field strength ($\mu_0 H$) at a constant microwave frequency of 9.4 GHz. The vertical bars on the peaks of the spectra mark the resonance field positions.

B. Experimental details

The bulk single-crystalline samples of $(\text{Fe}:\text{Ni}:\text{M})_3\text{P}$ ($M = \text{Ru}, \text{Pd}$) were synthesized by a self-flux method as reported in Refs. [53,54]. Magnetization was measured on single crystals using a superconducting quantum interference device (SQUID) magnetometer. The ferromagnetic transition temperature T_C decreases from 412 K to 337 and 392 K by substituting $(\text{Fe}_{0.63}\text{Ni}_{0.37})_3\text{P}$ with Ru or Pd, respectively. The saturation magnetization M_s decreases as well (see Ref. [54]).

In order to perform FMR measurements, the bulk single crystals were prepared in the form of cylindrical thin disks, where the values of the diameter/thickness ratio are 8.57, 3.14, and 5.6 for, respectively, the $(\text{Fe}_{0.63}\text{Ni}_{0.37})_3\text{P}$, $(\text{Fe}_{0.59}\text{Ni}_{0.32}\text{Ru}_{0.09})_3\text{P}$, and $(\text{Fe}_{0.62}\text{Ni}_{0.29}\text{Pd}_{0.09})_3\text{P}$ samples. Both [110] and [001] axes are parallel to the large cylindrical surfaces of the samples, i.e., they are perpendicular to the mantle. On the other hand, to study the basal-plane anisotropy, a single-crystalline sample of $(\text{Fe}_{0.63}\text{Ni}_{0.30}\text{Pd}_{0.07})_3\text{P}$ was shaped in a cylindrical disk, whose large circular surfaces contains [110] and $[1\bar{1}0]$ axes.

Angular-dependent FMR measurements were performed using a continuous-wave spectrometer (Bruker ELEXSYS E500A) at X-band frequency ($\nu = 9.4$ GHz), for selected temperatures 5, 50, 100, 150, 200, 250, 300, 350, and 380 K using a continuous helium gas-flow cryostat (Oxford Instruments) for $T \leq 300$ K and a nitrogen gas-flow cryostat (Bruker) for $T \geq 300$ K, respectively. The electromagnet covers a sweep field regime up to 1.6 T. The orientation of samples was controlled by a programmable goniometer in 5° steps during a full rotation of the magnetic field in the plane of the cylindrical disk.

FMR detects the power P_{abs} absorbed by the sample from the transverse magnetic microwave field as a function of the static magnetic field H . In the Bruker spectrometer, this is realized in reflection geometry and the signal-to-noise ratio of the spectra is improved by recording the derivative dP_{abs}/dH

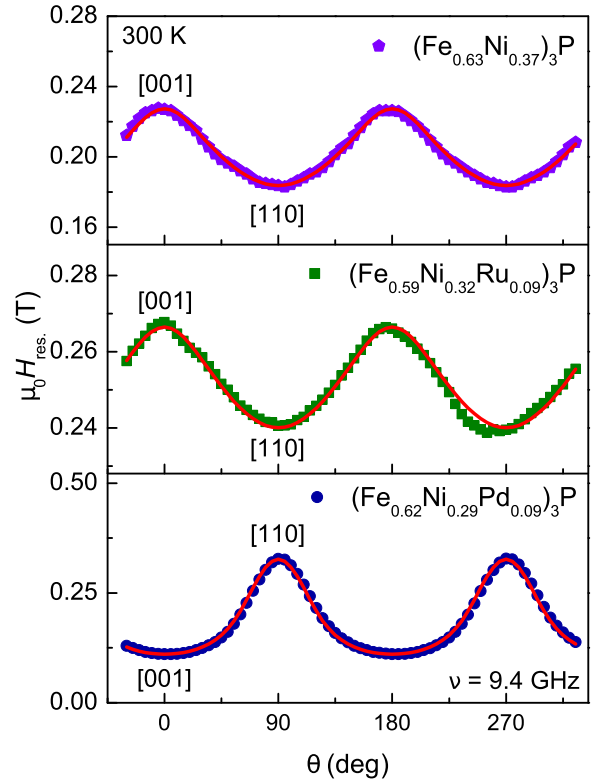


FIG. 4. Angular dependence of the resonance field of $(\text{Fe}_{0.63}\text{Ni}_{0.37})_3\text{P}$, $(\text{Fe}_{0.59}\text{Ni}_{0.32}\text{Ru}_{0.09})_3\text{P}$, and $(\text{Fe}_{0.62}\text{Ni}_{0.29}\text{Pd}_{0.09})_3\text{P}$ as measured at 300 K for $\nu = 9.4$ GHz. The first two compounds show an easy-plane type of magnetocrystalline anisotropy, while the third compound reveals an easy-axis anisotropy. The solid red lines depict the fits that are modeled by the uniaxial magnetocrystalline anisotropy, as described in the text. Maxima and minima correspond to hard and easy axes, respectively.

using a lock-in technique with field modulation. The integrated signals of dP_{abs}/dH dependent on the orientation of the magnetic field $\mu_0 H(\theta)$ exhibit maxima corresponding to the FMR resonance fields $\mu_0 H_{\text{res}}$, as depicted in Fig. 3 for $T = 300$ K.

The resonance field in both $(\text{Fe}_{0.63}\text{Ni}_{0.37})_3\text{P}$ and $(\text{Fe}_{0.59}\text{Ni}_{0.32}\text{Ru}_{0.09})_3\text{P}$ shifts to lower fields by a small amount of 46 and 22 mT, respectively, upon the rotation of the applied magnetic field within the disk from the [001] to [110] axes. On the contrary, the resonance field shifts to a significantly larger value (by about 217 mT) in $(\text{Fe}_{0.62}\text{Ni}_{0.29}\text{Pd}_{0.09})_3\text{P}$. This different behavior proves the easy-plane anisotropy of the former two compounds in contrast to the easy-axis anisotropy of the latter compound (Fig. 4). To evaluate the uniaxial magnetic anisotropy, the angular dependence of the resonance field data was fitted using Eq. (1).

III. RESULTS AND DISCUSSIONS

A. Temperature dependence of K_u

Starting with $(\text{Fe}_{0.63}\text{Ni}_{0.37})_3\text{P}$ with easy-plane anisotropy, the magnitude of K_1 decreases with increasing temperature with the values $K_1 = -33$ and -2 kJ/m³ at 5 and 380 K, respectively [Fig. 5(a)]. This implies that the anisotropy remains easy plane by temperatures approaching the

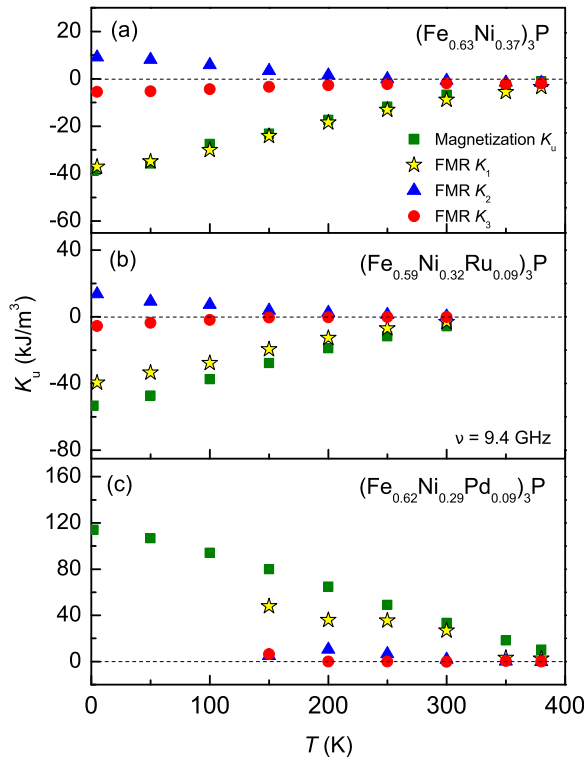


FIG. 5. Temperature dependence of the uniaxial anisotropy constants K_1 , K_2 , and K_3 kJ/m^3 for $(\text{Fe}_{0.63}\text{Ni}_{0.37})_3\text{P}$, $(\text{Fe}_{0.59}\text{Ni}_{0.32}\text{Ru}_{0.09})_3\text{P}$, and $(\text{Fe}_{0.62}\text{Ni}_{0.29}\text{Pd}_{0.09})_3\text{P}$ obtained by FMR at $\nu = 9.4$ GHz. The other plotted values of K_u kJ/m^3 are obtained by using magnetization measurements as given in Ref. [54].

ferromagnetic transition at $T_C = 412$ K. As shown in Fig. 5(a), the values of K_2 are positive and decreasing faster than those of K_1 , as the temperature increases. Moreover, the values of K_3 remain negative, but are generally close to zero within the experimental and analysis uncertainty. Following Eq. (4), the anisotropy field can be estimated as $\mu_0 H_{\text{ani}} = |2K_1/\mu_0 M_s| \approx 0.1$ T at 5 K, and decreases to 9 mT at 380 K. The isotropic g factor changes from 1.55 at 5 K to around 1.90 on the border of the paramagnetic phase. Note that this should be taken as an effective g factor because the observed shift probably results from the simplified assumption concerning the effective demagnetization factor of the metallic disk.

Similar to $(\text{Fe}_{0.63}\text{Ni}_{0.37})_3\text{P}$, the second-order anisotropy constant of $(\text{Fe}_{0.59}\text{Ni}_{0.32}\text{Ru}_{0.09})_3\text{P}$ reveals an easy-plane anisotropy character with $K_1 = -39.5$ kJ/m^3 , which monotonously increases to -3 kJ/m^3 on increasing temperature from 5 K up to the room temperature, respectively [Fig. 5(b)]. Like in the previous sample, K_2 attains positive values and already decreases to approximately zero below T_C . The anisotropy field becomes one order of magnitude smaller, from approximately 114 to 17 mT, as the temperature increases from 5 to 300 K. The isotropic g factor was found to increase from 1.47 to 1.97 as the temperature rises from 5 to 300 K.

However, in $(\text{Fe}_{0.62}\text{Ni}_{0.29}\text{Pd}_{0.09})_3\text{P}$, the situation looks different. It was mentioned in Ref. [54] that the compound $(\text{Fe}_{0.63}\text{Ni}_{0.33})_3\text{P}$ has reached the optimal doping where the easy-plane anisotropy K_u reaches its minimum such that

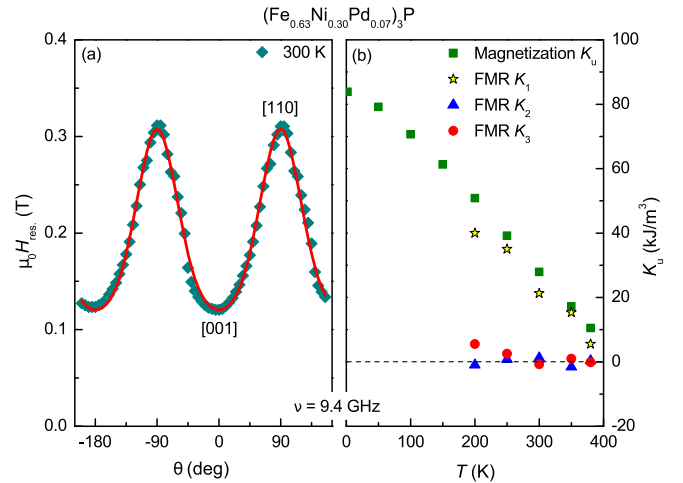


FIG. 6. (a) Angular dependence of the resonance field in the ac plane of $(\text{Fe}_{0.63}\text{Ni}_{0.30}\text{Pd}_{0.07})_3\text{P}$ at 300 K. (b) Temperature dependence of K_1 , K_2 , and K_3 kJ/m^3 values obtained by FMR at $\nu = 9.4$ GHz. The other plotted values of K_u kJ/m^3 are obtained by using magnetization measurements as given in Ref. [54].

the small amount of Pd (up to 4%) is enough to switch K_u from easy-plane to easy-axis anisotropy. Indeed, in $(\text{Fe}_{0.62}\text{Ni}_{0.29}\text{Pd}_{0.09})_3\text{P}$, all anisotropy constants K_1 , K_2 , and K_3 show positive values (easy-axis character), with very small deviations of K_2 , and K_3 toward negative values at 380 K [Fig. 5(c)]. The value of $K_1 = 48$ kJ/m^3 at 150 K drastically falls to about 2.5 kJ/m^3 at 380 K. The values of K_2 and K_3 are one to two orders of magnitude smaller than those of K_1 with respect to 150 and 380 K. The calculation of H_{ani} results in 154 mT at 150 K and 19 mT at 380 K. The corresponding isotropic g values are 1.50 and 1.71. The lack of X-band FMR data at temperatures lower than 150 K is due to the fact that at $\nu = 9.4$ GHz, we are below the full saturation range of the magnetization (around 0.6 T), as one can see in Ref. [54] where the spectra cannot be unambiguously evaluated.

The absolute values of K_1 as determined from the anisotropy of FMR in this work are slightly different from those of K_u obtained by magnetization measurements in Ref. [54]. These deviations cannot be recovered even by consideration of the values of higher orders K_2 and K_3 . This is mainly due to the fact that K_u was calculated from the difference of Helmholtz magnetic free energy along the [110] and [001] axes in which K_u is equal to the area enclosed by the magnetization curves along the above-mentioned directions. Although, in this case, the magnetization process along the easy axis is dominated by the displacement of domain walls, the contribution of this process was excluded in this formulation. In contrast, FMR experiments probe the dynamical modes of the magnetization in the saturated state. This means that domain walls do not play any role in this case. Therefore, a slight discrepancy between K_u and K_1 is expected.

The error bars have been estimated in a semiquantitative way: the fit parameters K_1 and K_2 were each varied as far to increase χ^2 by 10 percent away from its minimal value. Such deviations in χ^2 typically indicate a worse fit visible to the eye, but, on the other hand, they respect the failures of the eye to find the true minimum in χ^2 . In Figs. 5 and 6, all the error bars are large as the symbols.

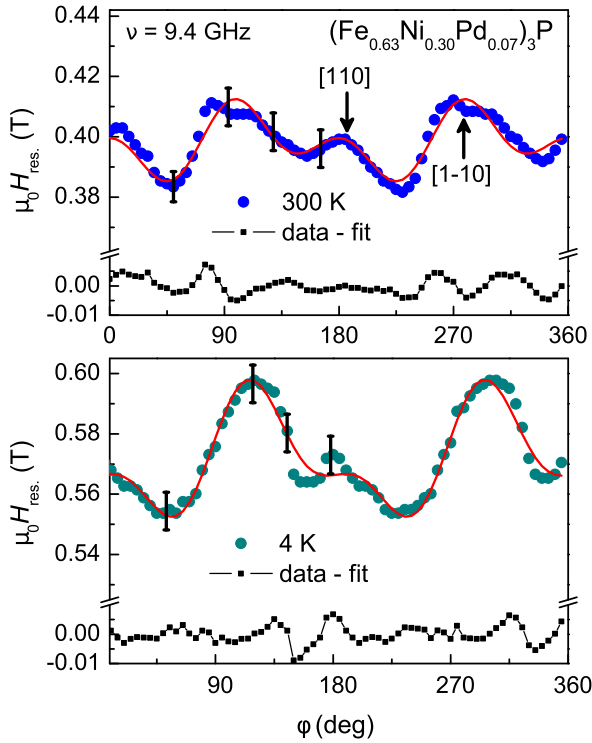


FIG. 7. Angular dependence of the resonance field in the ab plane of $(\text{Fe}_{0.63}\text{Ni}_{0.30}\text{Pd}_{0.07})_3\text{P}$ at 4 and 300 K. Besides the twofold symmetry due to slight tilting of the sample, it reveals the fourfold fourth-order anisotropy due to S_4 symmetry. The solid red lines describe the fit by Eq. (8). The black points at the bottom of each frame represent the difference between the data and fit.

B. Fourfold symmetry of planar anisotropy

1. FMR results

Recall the FMR data of $(\text{Fe}_{0.63}\text{Ni}_{0.30}\text{Pd}_{0.07})_3\text{P}$, where the angular dependence of the resonance field at different temperatures reveals an easy-axis type of anisotropy [Fig. 6(a)]. The evolution of K_u with temperature was discussed in Ref. [54]. The values of K_u , which are obtained by the Helmholtz method, were found to be in good agreement with our values of K_1 for higher temperatures ($T > 250$ K). Here we would like to point out that both K_2 and K_3 contributions would not make a large difference of the total K_u values [Fig. 6(b)]. At 300 K, $K_1 \approx 21$ kJ/m³. The corresponding anisotropy field $\mu_0 H_{\text{ani}} \approx 90$ mT.

On the other hand, Fig. 7 shows the angular dependence of the ferromagnetic resonance field ($\mu_0 H_{\text{res}}$) of $(\text{Fe}_{0.63}\text{Ni}_{0.30}\text{Pd}_{0.07})_3\text{P}$ for the magnetic field applied within the ab plane at 4 and 300 K. One can recognize the superposition of a twofold and a fourfold periodicity, which can be described with Eq. (8). Using the empirical value of $K_1/M_s \approx 59$ mT at 300 K, one obtains $\theta_t \approx 17^\circ$, $\varphi_t \approx 23^\circ$, $\varphi_b \approx 5^\circ$, and $K_b \approx -3$ kJ/m³. At 4 K with $K_1/M_s \approx 118$ mT, one obtains $\theta_t \approx 18^\circ$, $\varphi_t \approx 35^\circ$, $\varphi_b \approx 23^\circ$, and $K_b \approx 5$ kJ/m³. The difference plots at the bottom of each frame in Fig. 7 indicate deviations probably due to imperfections of the disk shape. Such imperfections lead to nonuniform demagnetization contributions, which are not important as compared to the strong anisotropy in the ac plane, but become obvious in the case of the weak basal anisotropy. The polar tilt angle θ_t is consistent for both

angular dependencies at 300 and 4 K within 1° , respectively. The uncertainty of the azimuthal tilt φ_t and basal angles φ_b is larger ($\pm 10^\circ$) because of the above-mentioned imperfections of the sample shape.

Nevertheless, a reasonable approximation of the basal anisotropy is obtained from fitting with Eq. (8). Regarding the error bars of the data points estimated by ($\pm 5\%$) of the resonance linewidth, the values of K_b exhibit an uncertainty of ($\pm 20\%$). Note that the K_b values are only about one order of magnitude smaller than those of K_u , as obtained in Ref. [54]. This result reveals that K_b in this compound is significantly larger than, for example, in GdRh_2Si_2 , which has a tetragonal structure and uniaxial symmetry as well [64].

2. Effect on magnetic textures

We examine the effect of the fourfold basal anisotropy on magnetic textures theoretically within a micromagnetic model. Apart from the anisotropies in Eq. (2), the energy functional comprises the magnetic stiffness A , Zeeman interaction with the external field \mathbf{B} , demagnetization energy, and S_4 -symmetric DMI D :

$$E = \int dV [A(\nabla \mathbf{m})^2 - M_s \mathbf{m} \cdot \mathbf{B} - M_s \mathbf{m} \cdot \mathbf{B}_{\text{dem}} + D \mathbf{m} \cdot (\hat{\mathbf{d}}_1 \times \partial_1 \mathbf{m} - \hat{\mathbf{d}}_2 \times \partial_2 \mathbf{m}) + K_1 \mathbf{m}_z^2 + K_b (\hat{\mathbf{b}}_1 \cdot \mathbf{m})^2 (\hat{\mathbf{b}}_2 \cdot \mathbf{m})^2]. \quad (9)$$

The orientation of the DMI is defined via the orthogonal vectors $\hat{\mathbf{d}}_1 = \cos \varphi_{\text{DM}} \hat{e}_{100} + \sin \varphi_{\text{DM}} \hat{e}_{010}$ and $\hat{\mathbf{d}}_2 = \hat{e}_{001} \times \hat{\mathbf{d}}_1$. The operator ∂_i denotes a derivative along $\hat{\mathbf{d}}_i$. For $D > 0$, this DMI favors a right-handed helix in $\hat{\mathbf{d}}_1$ and a left-handed helix in the $\hat{\mathbf{d}}_2$ direction. It is important to notice that the defining vectors of the basal anisotropy $\hat{\mathbf{b}}_i$ and the DMI $\hat{\mathbf{d}}_i$ are independent and their only symmetry-imposed constraint is the orientation perpendicular to $[001]$. This is different in magnets with D_{2d} symmetry, where both sets of vectors are by symmetry pinned to the $[100]$ and $[010]$ axes.

Let us now consider a domain wall separating regions with $\mathbf{m} = (0, 0, \pm 1)^T$ as the most simple noncollinear texture. Demagnetization energy forces the domain wall to have Bloch-type helicity deep in the bulk, with left and right handedness being energetically degenerate. As discussed in Ref. [53], for the DMI these handednesses are energetically favorable only in two orthogonal directions, here given by $\hat{\mathbf{d}}_1$ or $\hat{\mathbf{d}}_2$, respectively. However, the effect of basal anisotropy was neglected, which favors Bloch-type domain walls in the $\hat{\mathbf{b}}_1$ or $\hat{\mathbf{b}}_2$ direction, irrespective of handedness.

An analytical solution for the domain-wall orientation anisotropy can be obtained in the limit of negligible D and K_b , far away from the surfaces where the effect of dipolar interactions is pinning of the helicity to Bloch type. In this limit, the domain-wall profile $m_z = \cos \theta$ is given by $\theta(\mathbf{r}) = 2 \arctan\{\exp[-(\mathbf{r} \cdot \hat{n}_{\text{dw}})/\lambda]\}$, where $\lambda = \sqrt{A/|K_1|}$ is the characteristic length scale and \hat{n}_{dw} is the vector normal to the domain wall. The perturbative energies of basal anisotropy and DMI, assuming no deformation of the domain-wall profile, read

$$E_{K_b} = \frac{1}{3} \lambda K_b \sin^2[2(\varphi_b - \varphi_{\text{dw}})],$$

$$E_{\text{DMI}} = -\pi D |\cos[2(\varphi_{\text{DM}} - \varphi_{\text{dw}})]|. \quad (10)$$

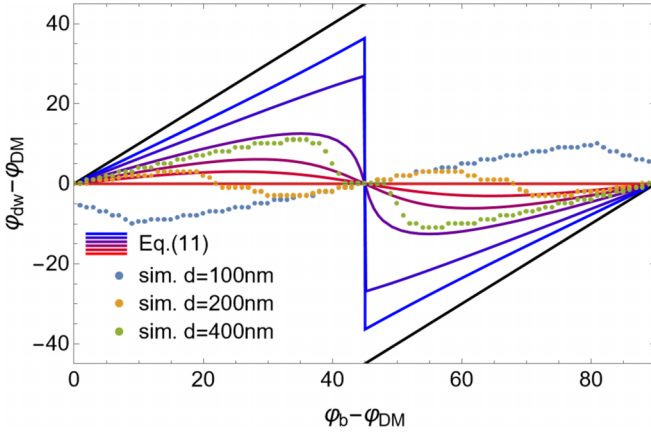


FIG. 8. Angle between the lowest-energy domain-wall orientation φ_{dw} and the DMI axis orientation φ_{DM} as a function of the basal anisotropy orientation φ_b (relative to φ_{DM}). Colored lines show the perturbative result of a simple model, given by Eq. (10), for different values of the ratio between DMI D and basal anisotropy K_b , i.e., $\sqrt{\frac{A}{|K_1|}} \frac{K_b}{D} = 0, 1, 2, 4, 8, 16$, from red to blue. The black line indicates the limit $\varphi_{dw} = \varphi_b$. The dots show numerically obtained results explained in the main text.

The absolute value in E_{DM} stems from jumps between left and right handedness. The domain-wall orientation with the smallest energy according to this simple perturbative model is shown in Fig. 8, obtained by numerically minimizing the total $E_{Kb} + E_{DM}$ of Eq. (10). The color encodes different values of the only dimensionless parameter $\lambda \frac{K_b}{D}$. The domain-wall orientation follows (i) the DMI orientation if the DMI is dominant (red limit) or (ii) the orientation of the basal anisotropy if K_b is dominant (blue/black limit). If both interactions are of comparable scale, the resulting domain-wall angle can take any intermediate value.

Additionally, we computed the energy of a domain-wall pair using a modified version of MUMAX3 [65], which features an improved numerical discretization scheme to avoid anisotropy effects of the numerical lattice, DMI of S_4 type with an arbitrary orientation in the xy plane, and basal anisotropy, as defined in Eq. (9). The results shown in Fig. 8 are calculated for different thicknesses as indicated and the standard parameters for $(\text{Fe}_{0.63}\text{Ni}_{0.30}\text{Pd}_{0.07})_3\text{P}$, i.e., $A = 8.1$ pJ/m, $D = 0.2$ mJ/m², $M_s = 417$ kA/m, and $K_u = -31$ kJ/m³ (note the different sign convention), as used in Ref. [53] for samples at $T = 300$ K. The pair of domain walls was discretized on $128 \times 128 \times 64$ lattice sites with periodic boundary conditions in the x and y directions (with 16 repeats using standard MUMAX3 procedures for the demagnetization). For every thickness, we first determined the system size at $D = 0$ and $K_b = 0$ with the lowest-energy density. Next, we added the DMI as well as a basal anisotropy of $K_b = 25$ kJ/m³ which corresponds to $\lambda \frac{K_b}{D} \approx 2$. We also considered the more realistic case $K_b = 2.5$ kJ/m³, but modulations of the domain-wall orientation were only of the order of one degree. Similarly, the experimentally determined value $K_b = 3.66$ kJ/m³ ($\lambda \frac{K_b}{D} \approx 0.3$) at room temperature suggests that the effect on the domain-wall orientation can be expected to be

small. It turns out that in the case of real three-dimensional (3D) samples, where the domain walls become Néel type at the surfaces, the simple perturbative result breaks down. The energetically optimal orientation angle of the domain walls does not only depend on the orientation angles of the DMI and basal anisotropy as well as their relative strength, but it also strongly depends on the film thickness, including a sign change for most relative angles between the DMI and basal anisotropy. More sophisticated models or simulations are required to fully understand the interplay of basal anisotropy and anisotropic DMI and their combined effect on the orientation of domain walls.

The effect on more complex magnetic textures can be estimated based on these results for domain walls. In the limit $K_b = 0$, the antiskyrmions are square shaped, while skyrmions are elliptical [53]. In the opposite limit, $D = 0$, one can expect that both antiskyrmions and skyrmions are square shaped as their helical domain-wall regions are pinned in orthogonal directions. In the competing scenario, where both interactions are at work on similar scales, one may expect a trivial crossover or the emergence of more complicated shapes, depending on the relative strength of the interactions, their relative angle, and the thickness of the sample. The detailed numerical investigation of this rich phase diagram is, however, beyond the scope of the present work.

It is interesting to compare the situation for D_{2d} symmetry: In that case, the DMI axes $\hat{\mathbf{d}}_1$ and $\hat{\mathbf{d}}_2$ are oriented along the [100] and [010] directions, respectively, i.e., the same directions like the basal anisotropy axes $\hat{\mathbf{b}}_1$ and $\hat{\mathbf{b}}_2$. Thus, the orientation effects are limited to the trivial case $\varphi_b - \varphi_{DM} = 0$. In turn, the present S_4 -symmetric compound is astonishingly close to the opposite limit, $\varphi_b - \varphi_{DM} \approx 45^\circ$, which is the maximum mutual twist angle promoting the competition between both contributions to anisotropy.

We conclude that there is a rich zoo of effects emerging from the interplay of DMI and basal anisotropy, which can potentially be accessed experimentally by tuning the thickness of samples, the orientation of DMI and anisotropy axes by varying dopants, or the relative strength between interactions by varying doping concentrations or temperature, as different scaling relations may be expected for the different interactions. This rich variety of tuning knobs offers great potential for future investigations.

IV. CONCLUSIONS

We have successfully performed systematic FMR measurements on high-quality samples of several novel schreibersite compounds $(\text{Fe}_{0.63}\text{Ni}_{0.37})_3\text{P}$, $(\text{Fe}_{0.59}\text{Ni}_{0.32}\text{Ru}_{0.09})_3\text{P}$, and $(\text{Fe}_{0.62}\text{Ni}_{0.29}\text{Pd}_{0.09})_3\text{P}$ in order to study the behavior of the uniaxial anisotropy K_u as a function of temperature. In the two former compounds, the leading uniaxial parameter K_1 exhibits an easy-plane character, while in the latter, it shows an easy-axis character. These results are in fair agreement with previously obtained results for K_u using a magnetization measurement technique. Moreover, our FMR measurements allowed us to determine the higher-order anisotropy parameters K_2 and K_3 . K_2 turned out to be positive for all three compounds, with absolute values one order of magnitude smaller

than the corresponding K_1 . K_3 is again one order of magnitude smaller than K_2 , but its sign basically follows that of K_1 .

In addition, we studied the planar anisotropy K_b in $(\text{Fe}_{0.63}\text{Ni}_{0.30}\text{Pd}_{0.07})_3\text{P}$ by means of FMR. The results proof a fourfold symmetry as expected for the tetragonal crystal structure. The value of the corresponding anisotropy parameter K_b is an order of magnitude smaller than that of K_u . Our micromagnetic simulations reveal that a basal anisotropy can indeed influence the orientation of domain walls and the stripe phase, and is likely to also affect the shape of skyrmions and antiskyrmions, if the basal anisotropy competes with the DMI. However, the actual strength of K_b is at least one order of magnitude too small to provoke sizable effects.

Please refer to Ref. [66] for the simulation code used in this paper.

ACKNOWLEDGMENTS

This work was partially supported by the Deutsche Forschungsgemeinschaft (DFG) within the Transregional Collaborative Research Center TRR 360 “Constrained Quantum Matter”, Project No. 492547816 (Augsburg, Munich, Stuttgart, Leipzig) and via the DFG Priority Program SPP2137, Skyrmionics, under Grant No. KE 2370/1-1. M.H. and H.-A.K.v.N. acknowledge funding within the joint RFBR-DFG research project, Contracts No. 19-51-45001 and No. KR2254/3-1. J.M. acknowledges financial support by the Alexander von Humboldt foundation as a Feodor Lynen Return Fellow. K.K. and Y.T. acknowledge funding by JSPS Grants-in-Aid for Scientific Research (Grants No. 23H01841 and No. 20K15164) and JST CREST (Grants No. JP-MJCR20T1 and No. JPMJCR1874).

- [1] I. Dzyaloshinsky, A thermodynamic theory of weak ferromagnetism of antiferromagnetics, *J. Phys. Chem. Solids* **4**, 241 (1958).
- [2] T. Moriya, New mechanism of anisotropic superexchange interaction, *Phys. Rev. Lett.* **4**, 228 (1960).
- [3] S. Mühlbauer, B. Binz, F. Jonietz, C. Pfleiderer, A. Rosch, A. Neubauer, R. Georgii, and P. Böni, Skyrmion lattice in a chiral magnet, *Science* **323**, 915 (2009).
- [4] J. Kindervater, T. Adams, A. Bauer, F. X. Haslbeck, A. Chacon, S. Mühlbauer, F. Jonietz, A. Neubauer, U. Gasser, G. Nagy, N. Martin, W. Häußler, R. Georgii, M. Garst, and C. Pfleiderer, Evolution of magnetocrystalline anisotropies in $\text{Mn}_{1-x}\text{Fe}_x\text{Si}$ and $\text{Mn}_{1-x}\text{Co}_x\text{Si}$ as inferred from small-angle neutron scattering and bulk properties, *Phys. Rev. B* **101**, 104406 (2020).
- [5] N. Josten, T. Feggeler, R. Meckenstock, D. Spoddig, M. Spasova, K. Chai, I. Radulov, Z.-A. Li, O. Gutfleisch, M. Farle, and B. Zingsem, Dynamic unidirectional anisotropy in cubic FeGe with antisymmetric spin-spin-coupling, *Sci. Rep.* **10**, 2861 (2020).
- [6] A. Chacon, L. Heinen, M. Halder, A. Bauer, W. Simeth, S. Mühlbauer, H. Berger, M. Garst, A. Rosch, and C. Pfleiderer, Observation of two independent skyrmion phases in a chiral magnetic material, *Nat. Phys.* **14**, 936 (2018).
- [7] A. O. Leonov, C. Pappas, and I. Kézsmárki, Field and anisotropy driven transformations of spin spirals in cubic skyrmion hosts, *Phys. Rev. Res.* **2**, 043386 (2020).
- [8] M. Preißinger, K. Karube, D. Ehlers, B. Szigeti, H.-A. Krug von Nidda, J. S. White, V. Ukleev, H. M. Rønnow, Y. Tokunaga, A. Kikawa, Y. Tokura, Y. Taguchi, and I. Kézsmárki, Vital role of magnetocrystalline anisotropy in cubic chiral skyrmion hosts, *npj Quantum Mater.* **6**, 65 (2021).
- [9] X. Yu, M. Mostovoy, Y. Tokunaga, W. Zhang, K. Kimoto, Y. Matsui, Y. Kaneko, N. Nagaosa, and Y. Tokura, Magnetic stripes and skyrmions with helicity reversals, *Proc. Natl. Acad. Sci. USA* **109**, 8856 (2012).
- [10] W. Wang, Y. Zhang, G. Xu, L. Peng, B. Ding, Y. Wang, Z. Hou, X. Zhang, X. Li, E. Liu, S. Wang, J. Cai, F. Wang, J. Li, F. Hu, G. Wu, B. Shen, X.-X. Zhang, A centrosymmetric hexagonal magnet with superstable biskyrmion magnetic nanodomains in a wide temperature range of 100–340 K, *Adv. Mater.* **28**, 6887 (2016).
- [11] X. Yu, Y. Tokunaga, Y. Taguchi, and Y. Tokura, Variation of topology in magnetic bubbles in a colossal magnetoresistive manganite, *Adv. Mater.* **29**, 1603958 (2017).
- [12] M. Althaler, E. Lysne, E. Roede, L. Prodan, V. Tsurkan, M. A. Kassem, H. Nakamura, S. Krohns, István Kézsmárki, and D. Meier, Magnetic and geometric control of spin textures in the itinerant kagome magnet Fe_3Sn_2 , *Phys. Rev. Res.* **3**, 043191 (2021).
- [13] T. Okubo, S. Chung, and H. Kawamura, Multiple- q states and the skyrmion lattice of the triangular-lattice Heisenberg antiferromagnet under magnetic fields, *Phys. Rev. Lett.* **108**, 017206 (2012).
- [14] S. Hayami, S. Z. Lin, and C. D. Batista, Bubble and skyrmion crystals in frustrated magnets with easy-axis anisotropy *Phys. Rev. B* **93**, 184413 (2016).
- [15] Y. Hu, X. Chi, X. Li, Y. Liu, and A. Du, Creation and annihilation of skyrmions in the frustrated magnets with competing exchange interactions, *Sci. Rep.* **7**, 16079 (2017).
- [16] T. Kurumaji, T. Nakajima, M. Hirschberger, A. Kikkawa, Y. Yamasaki, H. Sagayama, H. Nakao, Y. Taguchi, T.-H. Arima, and Y. Tokura, Skyrmion lattice with a giant topological Hall effect in a frustrated triangular-lattice magnet, *Science* **365**, 914 (2019).
- [17] M. Hirschberger, T. Nakajima, S. Gao, L. Peng, A. Kikkawa, T. Kurumaji, M. Kriener, Y. Yamasaki, H. Sagayama, H. Nakao, K. Ohishi, K. Kakurai, Y. Taguchi, X. Yu, T.-H. Arima, and Y. Tokura, Skyrmion phase and competing magnetic orders on a breathing kagomé lattice, *Nat. Commun.* **10**, 5831 (2019).
- [18] A. N. Bogdanov and D. A. Yablonskiĭ, Thermodynamically stable vortices in magnetically ordered crystals. The mixed state of magnets, *Zh. Éksp. Teor. Fiz.* **95**, 178 (1989) [*Sov. Phys. JETP* **68**, 101 (1989)].
- [19] I. Kézsmárki, S. Bordács, P. Milde, E. Neuber, L. M. Eng, J. S. White, H. M. Rønnow, C. D. Dewhurst, M. Mochizuki, K. Yanai, H. Nakamura, D. Ehlers, V. Tsurkan, and A. Loidl, Néel-type skyrmion lattice with confined orientation in the polar magnetic semiconductor GaV_4S_8 , *Nat. Mater.* **14**, 1116 (2015).
- [20] D. Ehlers, I. Stasinopoulos, V. Tsurkan, H.-A. Krug von Nidda, T. Fehér, A. Leonov, I. Kézsmárki, D. Grundler, and A. Loidl, Skyrmion dynamics under uniaxial anisotropy, *Phys. Rev. B* **94**, 014406 (2016).

- [21] D. Ehlers, I. Stasinopoulos, I. Kézsmárki, T. Fehér, V. Tsurkan, H.-A. Krug von Nidda, D. Grundler, and A. Loidl, Exchange anisotropy in the skyrmion host GaV_4S_8 , *J. Phys.: Condens. Matter* **29**, 065803 (2017).
- [22] S. Bordács, A. Butykai, B. G. Szigeti, J. S. White, R. Cubitt, A. O. Leonov, S. Widmann, D. Ehlers, H.-A. Krug von Nidda, V. Tsurkan, A. Loidl, and I. Kézsmárki, Equilibrium skyrmion lattice ground state in a polar easy-plane magnet, *Sci. Rep.* **7**, 7584 (2017).
- [23] Á. Butykai, K. Geirhos, D. Szaller, L. F. Kiss, L. Balogh, M. Azhar, M. Garst, L. DeBeer-Schmitt, T. Waki, Y. Tabata, H. Nakamura, I. Kézsmárki, and S. Bordács, Squeezing the periodicity of Néel-type magnetic modulations by enhanced Dzyaloshinskii-Moriya interaction of $4d$ electrons, *npj Quantum Mater.* **7**, 26 (2022).
- [24] T. J. Hicken, S. J. R. Holt, K. J. A. Franke, Z. Hawkhead, A. Štefančič, M. N. Wilson, M. Gomilšek, B. M. Huddart, S. J. Clark, M. R. Lees, F. L. Pratt, S. J. Blundell, G. Balakrishnan, and T. Lancaster, Magnetism and Néel skyrmion dynamics in $\text{GaV}_4\text{S}_{8-y}\text{Se}_y$, *Phys. Rev. Res.* **2**, 032001(R) (2020).
- [25] K. Geirhos, S. Reschke, S. Ghara, S. Krohns, P. Lunkenheimer, and I. Kézsmárki, Optical, dielectric, and magnetoelectric properties of ferroelectric and antiferroelectric lacunar spinels, *Phys. Status Solidi B* **259**, 2100160 (2022).
- [26] A. K. Nayak, V. Kumar, T. Ma, P. Werner, E. Pippel, R. Sahoo, F. Damay, U. K. Röbber, C. Felser, and S. S. P. Parkin, Magnetic antiskyrmions above room temperature in tetragonal Heusler materials, *Nature (London)* **548**, 561 (2017).
- [27] R. Saha, A. K. Srivastava, T. Ma, J. Jena, P. Werner, V. Kumar, C. Felser, and S. S. P. Parkin, Intrinsic stability of magnetic antiskyrmions in the tetragonal inverse Heusler compound $\text{Mn}_{1.4}\text{Pt}_{0.9}\text{Pd}_{0.1}\text{Sn}$, *Nat. Commun.* **10**, 5305 (2019).
- [28] S. Sen, C. Singh, P. K. Mukharjee, R. Nath, and A. K. Nayak, Observation of the topological Hall effect and signature of room-temperature antiskyrmions in Mn-Ni-Ga D_{2d} Heusler magnets, *Phys. Rev. B* **99**, 134404 (2019).
- [29] W.-Y. Choi, W. Yoo, and M.-H. Jung, Emergence of the topological Hall effect in a tetragonal compensated ferrimagnet $\text{Mn}_{2.3}\text{Pd}_{0.7}\text{Ga}$, *NPG Asia Mater* **13**, 79 (2021).
- [30] M. N. Wilson, T. J. Hicken, M. Gomilšek, A. Štefančič, G. Balakrishnan, J. C. Loudon, A. C. Twitchett-Harrison, F. L. Pratt, M. Telling, and T. Lancaster, Spin dynamics in bulk MnNiGa and $\text{Mn}_{1.4}\text{Pt}_{0.9}\text{Pd}_{0.1}\text{Sn}$ investigated by muon spin relaxation, *Phys. Rev. B* **104**, 134414 (2021).
- [31] S. Sen, K. Somesh, R. Nath, and A. K. Nayak, Manipulation of antiskyrmion phase in $\text{Mn}_{2+x}\text{Ni}_{1-x}\text{Ga}$ tetragonal Heusler system, *Phys. Rev. Appl.* **17**, 044040 (2022).
- [32] A. Neubauer, C. Pfleiderer, B. Binz, A. Rosch, R. Ritz, P. G. Niklowitz, and P. Böni, Topological Hall effect in the A phase of MnSi , *Phys. Rev. Lett.* **102**, 186602 (2009).
- [33] F. Jonietz, S. Mühlbauer, C. Pfleiderer, A. Neubauer, W. Münzer, A. Bauer, T. Adams, R. Georgi, P. Böni, R. A. Duine, K. Everschor, M. Garst, and A. Rosch, Spin transfer torques in MnSi at ultralow current densities, *Science* **330**, 1648 (2010).
- [34] V. Bonbien, F. Zhuo, A. Salimath, O. Ly, A. About, and A. Manchon, Topological aspects of antiferromagnets, *J. Phys. D: Appl. Phys.* **55**, 103002 (2022).
- [35] P. Swekis, A. Markou, D. Kriegner, J. Gayles, R. Schlitz, W. Schnelle, S. T. B. Goennenwein, and C. Felser, Topological Hall effect in thin films of $\text{Mn}_{1.5}\text{PtSn}$, *Phys. Rev. Mater.* **3**, 013001(R) (2019).
- [36] U. Ritzmann, S. v. Malotki, J.-V. Kim, S. Heinze, J. Sinova, and B. Dupé, Trochoidal motion and pair generation in skyrmion and antiskyrmion dynamics under spin-orbit torques, *Nat. Electron.* **1**, 451 (2018).
- [37] P. Vir, J. Gayles, A. S. Sukhanov, N. Kumar, F. Damay, Y. Sun, J. Kübler, C. Shekhar, and C. Felser, Anisotropic topological Hall effect with real and momentum space Berry curvature in the antiskyrmion-hosting Heusler compound $\text{Mn}_{1.4}\text{PtSn}$, *Phys. Rev. B* **99**, 140406(R) (2019).
- [38] A. S. Sukhanov, B. E. Zuniga Cespedes, P. Vir, A. S. Cameron, A. Heinemann, N. Martin, G. Chaboussant, V. Kumar, P. Milde, L. M. Eng, C. Felser, and D. S. Inosov, Anisotropic fractal magnetic domain pattern in bulk $\text{Mn}_{1.4}\text{PtSn}$, *Phys. Rev. B* **102**, 174447 (2020).
- [39] P. Swekis, J. Gayles, D. Kriegner, G. H. Fecher, Y. Sun, S. T. B. Goennenwein, C. Felser, and A. Markou, Role of magnetic exchange interactions in chiral-type Hall effects of epitaxial Mn_xPtSn films, *ACS Appl. Electron. Mater.* **3**, 1323 (2021).
- [40] V. Kumar, N. Kumar, M. Reehuis, J. Gayles, A. S. Sukhanov, A. Hoser, F. Damay, Ch. Shekhar, P. Adler, and C. Felser, Detection of antiskyrmions by topological Hall effect in Heusler compounds, *Phys. Rev. B* **101**, 014424 (2020).
- [41] S. Sugimoto, Y. Takahashi, and S. Kasai, Transition of topological Hall effect for tetragonal Heusler Mn_2PtSn thin film, *Appl. Phys. Express* **14**, 103003 (2021).
- [42] P. Swekis, A. Markou, J. Sichelschmidt, C. Felser, and S. T. B. Goennenwein, Magnetocrystalline anisotropies in Mn_xPtSn thin films, *APL Mater.* **9**, 051104 (2021).
- [43] S. Hayami and Y. Motome, Effect of magnetic anisotropy on skyrmions with a high topological number in itinerant magnets, *Phys. Rev. B* **99**, 094420 (2019).
- [44] D. Bhattacharya, S. A. Razavi, H. Wu, B. Dai, K. L. Wang, and J. Atulasimha, Creation and annihilation of nonvolatile fixed magnetic skyrmions using voltage control of magnetic anisotropy, *Nat. Electron.* **3**, 539 (2020).
- [45] G. Pradhan, B. Ojha, and S. Bedanta, Effect of random anisotropy in stabilization of skyrmions and antiskyrmions, *J. Magn. Magn. Mater.* **528**, 167805 (2021).
- [46] L. Camosi, S. Rohart, O. Fruchart, S. Pizzini, M. Belmeguenai, Y. Roussigné, A. Stashkevich, S. M. Cherif, L. Ranno, M. de Santis, and J. Vogel, Anisotropic Dzyaloshinskii-Moriya interaction in ultrathin epitaxial $\text{Au/Co/W}(110)$, *Phys. Rev. B* **95**, 214422 (2017).
- [47] L. Camosi, N. Rougemaille, O. Fruchart, J. Vogel, and S. Rohart, Micromagnetics of antiskyrmions in ultrathin films, *Phys. Rev. B* **97**, 134404 (2018).
- [48] T. Ma, A. K. Sharma, R. Saha, A. K. Srivastava, P. Werner, P. Vir, V. Kumar, C. Felser, and S. S. P. Parkin, Tunable magnetic antiskyrmion size and helical period from nanometers to micrometers in a D_{2d} Heusler compound, *Adv. Mater.* **32**, 2002043 (2020).
- [49] J. Jena, R. Stinshoff, R. Saha, A. K. Srivastava, T. Ma, H. Deniz, P. Werner, C. Felser, and S. S. P. Parkin, Observation of magnetic antiskyrmions in the low magnetization ferrimagnet $\text{Mn}_2\text{Rh}_{0.95}\text{Ir}_{0.05}\text{Sn}$, *Nano Lett.* **20**, 59 (2020).

- [50] A. Ross, R. Lebrun, C. Ulloa, D. A. Grave, A. Kay, L. Baldrati, F. Kronast, S. Valencia, A. Rothschild, and M. Kläui, Structural sensitivity of the spin Hall magnetoresistance in antiferromagnetic thin films, *Phys. Rev. B* **102**, 094415 (2020).
- [51] S. Sandhoefner, A. Raeliarijaona, R. Nepal, D. Snyder-Tinoco, and A. A. Kovalev, Regular and in-plane skyrmions and antiskyrmions from boundary instabilities, *Phys. Rev. B* **104**, 064417 (2021).
- [52] P. Siegl, M. Stier, A. F. Schäffer, E. Y. Vedmedenko, T. Posske, R. Wiesendanger, and M. Thorwart, Creating arbitrary sequences of mobile magnetic skyrmions and antiskyrmions, *Phys. Rev. B* **106**, 014421 (2022).
- [53] K. Karube, L. Peng, J. Masell, X. Yu, F. Kagawa, Y. Tokura, and Y. Taguchi, Room-temperature antiskyrmions and sawtooth surface textures in a non-centrosymmetric magnet with S_4 symmetry, *Nat. Mater.* **20**, 335 (2021).
- [54] K. Karube, L. Peng, J. Masell, M. Hemmida, H.-A. Krug von Nidda, I. Kézsmárki, X. Yu, Y. Tokura, and Y. Taguchi, Doping control of magnetic anisotropy for stable antiskyrmion formation in schreibersite $(\text{Fe, Ni})_3\text{P}$ with S_4 symmetry, *Adv. Mater.* **34**, 2108770 (2022).
- [55] L. Peng, K. V. Iakubovskii, K. Karube, Y. Taguchi, Y. Tokura, and X. Yu, Formation and control of zero-field antiskyrmions in confining geometries, *Adv. Sci.* **9**, 2202950 (2022).
- [56] K. Karube and Y. Taguchi, High-temperature noncentrosymmetric magnets for skyrmionics, *APL Mater.* **10**, 080902 (2022).
- [57] K. Karube, V. Ukleev, F. Kagawa, Y. Tokura, Y. Taguchi, and J. S. White, Unveiling the anisotropic fractal magnetic domain structure in bulk crystals of antiskyrmion host $(\text{Fe, Ni, Pd})_3\text{P}$ by small-angle neutron scattering, *J. Appl. Crystallogr.* **55**, 1392 (2022).
- [58] D. Nakamura, K. Karube, K. Matsuura, F. Kagawa, X. Yu, Y. Tokura, and Y. Taguchi, Transport signatures of magnetic texture evolution in a microfabricated thin plate of antiskyrmion-hosting $(\text{Fe, Ni, Pd})_3\text{P}$, *Phys. Rev. B* **108**, 104403 (2023).
- [59] J. Smit and H. G. Beljers, Ferromagnetic resonance absorption in $\text{BaFe}_{12}\text{O}_{19}$, *Philips Res. Rep.* **10**, 113 (1955).
- [60] H. Suhl, Ferromagnetic resonance in nickel ferrite between one and two kilomegacycles, *Phys. Rev.* **97**, 555 (1955).
- [61] J. A. Osborn, Demagnetizing factors of the general ellipsoid, *Phys. Rev.* **67**, 351 (1945).
- [62] E. D. T. d. Lacheisserie, M. Schlenker, and D. Gignoux, *Magnetism: Fundamentals* (Springer, New York, 2005).
- [63] Derek J. Craik, *Magnetism: Principles and Applications* (Wiley, New York, 1995).
- [64] D. Ehlers, K. Kliemt, C. Krellner, C. Geibel, and J. Sichelschmidt, Uniaxial and fourfold basal anisotropy in GdRh_2Si_2 , *J. Phys.: Condens. Matter* **32**, 495801 (2020).
- [65] A. Vansteenkiste, J. Leliaert, M. Dvornik, M. Helsen, F. G.-Sanchez, and B. Van Waeyenberge, The design and verification of MuMax3, *AIP Adv.* **4**, 107133 (2014).
- [66] See Supplemental Material at <http://link.aps.org/supplemental/10.1103/PhysRevB.110.054416> for simulation code.